

# **Unconfined lock-exchange gravity currents with variable lock width: laboratory experiments and shallow-water simulations**

Journal:	<i>Journal of Hydraulic Research</i>
Manuscript ID	TJHR-2016-0209.R4
Manuscript Type:	Research paper
Date Submitted by the Author:	n/a
Complete List of Authors:	Lombardi, Valentina; University of Roma Tre, Engineering Adduce, Claudia; University of Roma Tre, Engineering La Rocca, Michele; University of Roma Tre, Engineering
Keywords:	gravity currents, shallow water model, laboratory experiments, unconfined gravity currents, entrainment
JHR Keywords:	Two- dimensional models < Computational methods in hydro-environment research and fluid dynamics, Laboratory studies < Instrumentation, measurements and experimental methods, Stratified flows and density currents < Environmental Fluid Mechanics

SCHOLARONE™  
Manuscripts

1  
2  
3  
4  
5  
6  
7  
8  
9  
10  
11  
12  
13  
14  
15  
16  
17  
18  
19  
20  
21  
22  
23  
24  
25  
26  
27  
28  
29  
30  
31  
32  
33  
34  
35  
36  
37  
38  
39  
40  
41  
42  
43  
44  
45  
46  
47  
48  
49  
50  
51  
52  
53  
54  
55  
56  
57  
58  
59  
60

Unconfined lock-exchange gravity currents with variable lock width:  
laboratory experiments and shallow-water simulations

VALENTINA LOMBARDI, Research Assistant, *Department of Engineering, University of  
Roma Tre, via Vito Volterra 62, 00146, Rome, Italy*

Email: [valentina.lombardi@uniroma3.it](mailto:valentina.lombardi@uniroma3.it)

CLAUDIA ADDUCE (IAHR Member), Associate Professor, *Department of Engineering,  
University of Roma Tre, via Vito Volterra 62, 00146, Rome, Italy*

Email: [claudia.adduce@uniroma3.it](mailto:claudia.adduce@uniroma3.it) (author for correspondence)

MICHELE LA ROCCA, Full Professor, *Department of Engineering, University of Roma Tre,  
via Vito Volterra 62, 00146, Rome, Italy*

Email: [michele.larocca@uniroma3.it](mailto:michele.larocca@uniroma3.it)

*Running Head: Unconfined lock-exchange gravity currents*

# Unconfined lock-exchange gravity currents with variable lock width: laboratory experiments and shallow-water simulations

## ABSTRACT

In this paper the dynamics of unconfined gravity currents generated by a lock-exchange with variable lock width was investigated. The gravity currents were generated by density differences caused by a salinity gradient and were realized both numerically and experimentally. Several runs were carried out in order to study the role played by the lock width on the current dynamics. Numerical simulations were performed with a new single-layer, 2D, shallow-water model, which accounts for the dilution of the gravity current due to the entrained ambient fluid. By the comparison between experimental and numerical results, the relevant role played by the entrainment on the velocity propagation of the front emerges, mainly for the cases with a narrow lock. The effect of the lock width on the current dynamics was also highlighted: the lock chocks the flow causing a concentrated loss of mechanical energy and a consequent deceleration of the flow. Results show that the smaller is the lock, the larger is the loss of energy.

*Keywords:* Buoyancy-driven flows; density currents; laboratory studies; stratified flows; two-dimensional models

## 1 Introduction

The term “gravity current” denotes the buoyancy-driven motion of two fluid masses with different densities. If the density gradient arises from a difference in temperature or salinity, the resulting flow is called “compositional gravity current”, while if the density excess is provided by the presence of suspended solid particles the so-called “particle-driven gravity current” occurs, i.e. “turbidity current”. Gravity currents play an important role in many geophysical and industrial situations as reviewed by Simpson (1997) and Huppert (2006). Among natural flows an example of a gravity current driven by thermally controlled density gradient is the sea breeze wind, while oceanic overflows, the salt wedge propagations and river plumes are gravity flows generated by a salinity difference between two fluid masses. Kneller and Buckee (2000) focused their study on the structure and behaviour of particle-driven gravity currents, such as submarine turbidity flows and pyroclastic currents, which are the main agents of the sediment transport on land and oceans.

An example of a gravity current involved in industrial situations is the dispersion in the environment of a dense gas or liquid originated by a chemical leakage. Due to the catastrophic consequences that the accidental spreading of chemical substances can cause, the full understanding of the gravity currents behaviour is required to assess and minimize the risks.

1  
2  
3  
4  
5  
6  
7  
8  
9  
10  
11  
12  
13  
14  
15  
16  
17  
18  
19  
20  
21  
22  
23  
24  
25  
26  
27  
28  
29  
30  
31  
32  
33  
34  
35  
36  
37  
38  
39  
40  
41  
42  
43  
44  
45  
46  
47  
48  
49  
50  
51  
52  
53  
54  
55  
56  
57  
58  
59  
60

The lock-exchange technique, i.e. a sudden release of a finite-volume of dense fluid into a lighter ambient fluid, is often used to generate gravity currents. The typical facility required to carry out a lock-exchange experiment is a transparent Plexiglas tank divided into two reservoirs separated by a removable lock; one portion is filled with the denser fluid (i.e. lock fluid) while the other one is filled with a fluid with a lower density (i.e. ambient fluid). After the gate removal, the lock fluid is instantaneously released into the ambient fluid and a relative motion between the two layers with different densities arises: the dense current flows along the bottom of the tank, while the lighter surrounding fluid propagates in the opposite direction along the upper boundary. The described procedure has been used to perform laboratory gravity currents in different experimental configurations. Among several experimental investigations one can mention Ross, Linden, and Dalziel (2002) and Patterson, Simpson, and Dalziel (2006) who generated axisymmetric gravity currents by the lock-exchange technique. Planar lock-release gravity currents on sloping boundaries were studied by Dai (2013, 2015), Marleau, Flynn, and Sutherland (2014), Lombardi, Adduce, Sciortino, and La Rocca (2015), and Ottolenghi, Adduce, Inghilesi, Roman, and Armenio (2016b). Nogueira, Adduce, Alves, and Franca (2013, 2014) and La Rocca, Adduce, Sciortino, and Bateman Pinzon (2008) carried out a series of lock-exchange experiments to study the effect of bed roughness on the currents dynamics, for planar and unconfined gravity currents, respectively. In literature, gravity currents have been reproduced in the laboratory by using a continuous buoyancy source as well (Baines, 2001, 2005; Cenedese and Adduce, 2008, 2010; Yuan and Horner-Devine, 2013; Ottolenghi, Cenedese and Adduce, 2017a).

Many numerical studies used high resolution numerical models as LES (Bombardelli, Cantero, García and Buscaglia, 2009; Ooi, Costantinescu, and Weber, 2009; Tokyay, Costantinescu, and Meiburg, 2011; Ottolenghi, Adduce, Inghilesi, Armenio, and Roman, 2016a; Ottolenghi et al., 2016b; Ottolenghi, Adduce, Roman, Armenio, 2017b) and DNS (Cantero et al., 2006; Gonzalez-Juez, Meiburg, and Costantinescu, 2009; Dai, 2015) to investigate lock-release gravity currents.

Recently the Lattice-Boltzmann method has been successfully employed to solve multilayer shallow-water model for the simulation of lock-release gravity currents (La Rocca, Adduce, Lombardi, Sciortino, and Hinkelmann, 2012b; La Rocca, Prestininzi, Adduce, Sciortino, and Hinkelmann, 2013; Prestininzi, Sciortino, and La Rocca, 2013; Prestininzi, Sciortino, and La Rocca, 2014). Most of the models used in literature to reproduce gravity currents are based on the shallow-water approximation. Indeed, as a natural gravity current mainly develops on the horizontal plane, the shallow-water theory is appropriate in reproducing its dynamics (see Rottmann and Simpson, 1983; Shin, Dalziel, and Linden, 2004; La Rocca et al., 2008; Ungarish, 2009; Adduce, Sciortino, and Proietti, 2012; Lombardi et al., 2015).

To the authors' knowledge, most of the experiments and simulations reported in literature investigate channelized gravity currents forced to flow parallel to the lateral walls according to the tank shape. However, there are several natural and industrial flows in which the density current is allowed to freely propagate over an horizontal plane as the plume fronts outflowing from rivers into the seawater, the release of wastewater in correspondence of a point discharge into a lake or ocean, or the spreading of oil on the sea surface. The full understanding of unconfined dense currents is also important to study the interactions between sea and fresh water occurring in correspondence of a sea lock (Van Meerkerk, O'Mahoney, and Twerda, 2015).

Only few works investigated freely propagating density currents (La Rocca et al., 2008; La Rocca, Adduce, Sciortino, Bateman Pinzon, and Boniforti, 2012a; Yuan and Horner-Devine, 2013; Cantero, Balachandar, García, and Ferry, 2006). Yuan and Horner-Devine (2013) realized laboratory buoyant currents by a continuous freshwater source testing both confined and unconfined configurations focusing on the influence of the lateral spreading on the flow structure. Cantero, Balachandar, and García (2007) studied three-dimensional cylindrical currents characterized by different Reynolds number obtained by high resolved simulations and experimental observations.

In order to provide an innovative contribution to the literature on unconfined gravity currents, the aim of this work is to investigate the dynamics of freely propagating gravity currents realized by means of lock-exchange experiments with different lock widths. To the authors' best knowledge, the effect of a variation of the lock width  $d$  on the gravity current dynamics has not been reported in the literature so far. The considered gravity currents have been numerically reproduced by a 2D, shallow-water model, which accounts for the mixing between the gravity current and the ambient fluid. The numerical model has been developed improving the model of La Rocca et al. (2008), where the gravity current and the ambient fluid were treated as immiscible liquids. The mixing is modelled by introducing the entrainment terms in the motion equations. The comparison between experimental and numerical results permitted to get an insight on the dynamics of the considered gravity currents, particularly being concerned with the role played by the entrainment of ambient fluid.

This paper is structured as follows: the experimental facility and procedure are described in section 2, experimental results are shown in section 3, the mathematical model is formulated in section 4, the analysis of numerical results is discussed in section 5 and the conclusions are drawn in section 6.

1  
2  
3  
4  
5  
6  
7  
8  
9  
10  
11  
12  
13  
14  
15  
16  
17  
18  
19  
20  
21  
22  
23  
24  
25  
26  
27  
28  
29  
30  
31  
32  
33  
34  
35  
36  
37  
38  
39  
40  
41  
42  
43  
44  
45  
46  
47  
48  
49  
50  
51  
52  
53  
54  
55  
56  
57  
58  
59  
60

2   **Experimental apparatus**

Lock-exchange gravity currents were generated in a rectangular Perspex tank of length  $L = 2.35$  m, width  $b = 1.35$  m and height  $H_t = 0.3$  m at the Hydraulics Laboratory of the University of Roma Tre. The experimental facility is shown in Fig. 1. The tank was divided into two reservoirs by a fixed vertical barrier, provided with a removable lock of variable width  $d$  and placed at  $L_0 = 1.125$  m from the left wall of the tank. The left reservoir was filled with a solution of water and sodium chloride (NaCl) with initial density  $\rho_{01}$  (i.e. the heavy fluid), while the right one was filled with fresh water with density  $\rho_2$  (i.e. the ambient or light fluid). A defined volume of methylene blue dye was added to the heavy fluid in order to distinguish it from the light one during the execution of the experiment. The density measurements were performed by a pycnometer with an estimated uncertainty of 0.2 %. Both reservoirs were filled to the same height  $h_0$ . The experiment is carried out as follows: the lock is rapidly lifted by means of a pneumatic mechanism and the heavy fluid collapses under the light one, generating the gravity current. A charged coupled device camera, with a time resolution of 25 fps and a spatial resolution of  $576 \times 768$  pixels was placed on the top of the tank and focused on the experimental domain, in order to record the development of the gravity current on the horizontal plane. The time-space evolution of the current was determined by applying an image analysis technique based on the threshold method, as in La Rocca et al. (2008), Adduce et al. (2012) and Lombardi et al. (2015). Points belonging to the current profile (i.e. the interface between the two fluids) were determined by a threshold method within an error of 0.4 cm.

Twelve experiments were carried out with two different values of the initial density of the heavy fluid  $\rho_{01} = 1010$  and  $1030 \text{ kg/m}^3$ , two values of the initial height  $h_0 = 0.10$  and  $0.15$  m and three values of the lock width  $d = 0.136, 0.35$  and  $0.67$  m. The measured density values of the fresh water (i.e. ambient fluid) ranged between  $1000 \text{ kg/m}^3$  and  $1002 \text{ kg/m}^3$ , depending on the tap water hardness. Table 1 shows the full list of the initial experimental conditions and the dimensionless parameters  $\gamma = \rho_2/\rho_{01}$ ,  $\delta = d/b$ ,  $R_i$ .

The initial reduced gravity  $g_0'$ , the buoyancy velocity  $U_0$  and the initial Reynolds number  $R_i$  are defined as follows:

$$g_0' = g \frac{\rho_{01} - \rho_2}{\rho_{01}} \tag{1}$$

$$U_0 = \sqrt{g_0' h_0} \tag{2}$$

$$R_i = \frac{U_0 h_0}{\nu} \tag{3}$$

where  $\nu$  is the kinematic viscosity. The values of the initial Reynolds number  $R_i$  ensure that turbulent flows were generated for all the investigated experimental conditions.

### 3 Experimental results

The experimental gravity current is generated as soon as the lock (Fig. 1) is removed. The dense fluid collapses and spreads in the right portion of the tank, while the surrounding fluid (i.e. the fresh water) propagates in the opposite direction above the dense layer. The experiment is considered ended as soon as the interface between the fluids reaches one of the sidewalls of the tank, in order to avoid the effects of reflection waves, which could influence the investigated phenomena and affect the experimental results.

Figure 2 shows the typical top view of the flow at three different times after the lock removal. The investigated domain is the right volume of the tank, where the spreading of the dense current takes place. As seen from the top, the gravity current spreads radially developing the typical mushroom-like shape and maintaining the symmetry with respect to the tank centreline (Ross et al., 2002; La Rocca et al., 2008). It is possible to see the typical lobe and cleft instabilities that appear at the front of the gravity currents and are caused by the influence of the bottom boundary on the lower region of the leading edge of the front (Simpson, 1997). As observed by Yuan and Horner-Devine (2013), shear induced billows due to Kelvin-Helmoltz instabilities occurred at the interface between the two fluids. In particular, Yuan and Horner-Devine (2013) by means of the OTM (Optical Thickness Method) observed the billows behaving as a periodic oscillation of the plume thickness and confirmed the presence of Kelvin-Helmoltz instabilities by using a combined PIV (Particle Image Velocimetry) and PLIF (Planar Induced Fluorescence) technique. Although in the present work the spreading of a density current is analysed only by an image analysis technique from the top view of the tank, the periodical oscillation of Kelvin-Helmoltz billows can be qualitatively observed in the snapshots of the experiments. As pointed out by Yuan and Horner-Devine (2013) the billows are easier to be identified in the dynamical movie, while the still images make the observation of such structure less clear. However, it is possible to observe a brighter band parallel to the leading edge of the plume in Fig. 2c (indicated by arrows), which corresponds to the portion behind the billow at the current front.

In Fig. 3 the current profile measured by threshold method is shown for Run 2, Run 5 and Run 8 at different times. In particular, Fig. 3a-c shows the effect of the initial height of the lock fluid on the gravity current propagation for Run 2 and Run 5, performed with the same values of  $d = 0.136$  m and  $\rho_{01} = 1010$  kg/m<sup>3</sup>, but with different values of  $h_0$  (i.e.  $h_0 = 0.15$  m for Run 2 and  $h_0 = 0.10$  m for Run 5). Indeed as expected, the flow generated with a higher initial height (Run 2) travelled for any given time a longer distance than the current

with a lower value of  $h_0$  (Run 5). In Fig. 3d-f Run 2 is compared with Run 8 in order to highlight the influence of the initial density of the lock fluid. As Run 8 and Run 2 were carried out with  $\rho_{01} = 1030 \text{ kg/m}^3$  and  $\rho_{01} = 1010 \text{ kg/m}^3$  respectively, the density difference provides a higher driving force for Run 8 than for Run 2. As a consequence, Run 8 propagates faster than Run 2.

In Fig. 4 the evolution of the gravity current is shown for Run 9, Run 8, Run 7 (Fig. 4a-c) and for Run 6, Run 5, Run 4 (Fig. 4d-f), focusing on the effect produced by the variation of the lock width  $d$ . More specifically, Fig. 4a-c shows the experiments carried out with  $\rho_{01} = 1030 \text{ kg/m}^3$  and  $h_0 = 0.15 \text{ m}$ , while in Fig. 4d-f the runs performed with  $\rho_{01} = 1010 \text{ kg/m}^3$  and  $h_0 = 0.10 \text{ m}$  are displayed. Both in Fig. 4a-c and Fig. 4d-f the considered currents are realized with three different values of  $d = 0.136, 0.35$  and  $0.67 \text{ m}$ . During the first stage of development, Run 7 and Run 4 (i.e.  $d = 0.136 \text{ m}$ ) show a higher front speed along the tank centreline, as it can be observed by the advanced position of the gravity current in Fig. 4a and Fig. 4d, respectively. However, although a difference in the lock width caused a different behaviour during the current development, the runs performed keeping constant  $\rho_{01}$  and  $h_0$  and changing only the width  $d$  reached the same position along the tank centreline at the considered times shown in Figs. 4c and 4f.

Figure 5 provides the instantaneous position of the experimental gravity current front along the centreline of the tank (i.e. along the  $x$  direction) obtained from the images of the gravity current top view. The time  $t$  and the front position  $x_f$  are scaled as in La Rocca et al. (2008), Lombardi et al. (2015) and Rottmann and Simpson (1983):

$$T^* = \frac{t\sqrt{g'_0 h_0}}{L_0}; \quad x_f^* = \frac{x_f}{L_0} \quad (4)$$

Each subplot refers to the runs obtained keeping constant  $\rho_{01}$  and  $h_0$  in order to highlight the effect of the lock width  $d$  on the flow development. In Fig. 5 the currents produced with  $d = 0.67 \text{ m}$  (i.e. Run 3, Run 6, Run 9 and Run 12) show a behaviour similar to a planar gravity current during the slumping phase (Huppert and Simpson, 1980; Rottmann and Simpson, 1983). The propagation speed along the centreline is almost constant and therefore the front position can be well described as a linear function of time. On the contrary, for the runs performed with  $d = 0.35$  and  $0.135 \text{ m}$  the speed decreases as the leading edge propagates. Indeed the front position along the centreline becomes a non linear function of time: the front speed decreases with time, therefore the flow is decelerating and such a non-linearity becomes more evident as the lock width decreases.



#### 4 The mathematical model

The single layer shallow-water model of La Rocca et al. (2008) has been improved by introducing the entrainment terms in the motion equations and used as a simulation tool in this work. As fully discussed by Ungarish (2009), the motion of the ambient fluid above the gravity current can be neglected, if the thickness of the upper lighter layer is large as compared to that of the lower heavier layer. Since the currents presented here fulfil the condition provided by Ungarish (2009), the one-layer approximation can be considered reasonable to model the flows investigated in the present study.

A sketch of the reference system of the model is shown in Fig. 6. The heavy fluid is a solution of tap water (density  $\rho_2$ ) and salt (density  $\rho_s$ ), whose density  $\rho_1$  depends on the concentration of salt and is expressed as:

$$\rho_1 = \rho_2 + (\rho_s - \rho_2)C \quad (5)$$

$C$  is the depth-averaged concentration of salt and is defined as cubic meters of salt per cubic meter of water. In this work NaCl has been used as salt. The following equations are obtained:

$$\begin{cases} \frac{\partial h_1}{\partial t} + \frac{\partial U h_1}{\partial x} + \frac{\partial V h_1}{\partial y} = \alpha U_m \\ \frac{\partial U h_1}{\partial t} + \frac{\partial}{\partial x} \left( U^2 h_1 + \frac{(\rho_s - \rho_2)g}{\rho_2} C \frac{h_1^2}{2} \right) + \frac{\partial UV h_1}{\partial y} = \alpha U U_m + \frac{1}{\rho_1} T_{xz} \Big|_{z=0} \\ \frac{\partial V h_1}{\partial t} + \frac{\partial UV h_1}{\partial x} + \frac{\partial}{\partial y} \left( V^2 h_1 + \frac{(\rho_s - \rho_2)g}{\rho_2} C \frac{h_1^2}{2} \right) = \alpha V U_m + \frac{1}{\rho_1} T_{yz} \Big|_{z=0} \\ \frac{\partial C h_1}{\partial t} + \frac{\partial C U h_1}{\partial x} + \frac{\partial C V h_1}{\partial y} = \alpha C U_m \end{cases} \quad (6)$$

where  $U$  and  $V$  are the depth-averaged velocity components along  $x$  and  $y$  axis, respectively, and  $h_1$  is the height of the dense fluid. While in La Rocca et al. (2008) a single-layer shallow water model for immiscible fluids was developed, the present model was improved accounting for the entrainment of ambient fluid. The entrainment is modelled using the following definition for the entrainment coefficient  $\alpha$  (Adduce et al., 2012):

$$\alpha = \frac{k \cdot F^2}{5 + F^2} \quad (7)$$

The densimetric Froude number  $F$  is defined as:

$$F = \frac{U_m}{\sqrt{gCh\left(\frac{\rho_s - \rho_2}{\rho_2}\right)}} \tag{8}$$

where  $U_m$  is the velocity modulus:

$$U_m = \sqrt{U^2 + V^2} \tag{9}$$

The value of the parameter  $k$  in equation (8) is set to 0.06 on the basis of previous entrainment evaluations of Nogueira et al. (2014) and Ottolenghi et al. (2016a,b).

The stress terms at the bottom, assumed flat, are defined as:

$$\begin{cases} \frac{1}{\rho_1} T_{xz}|_{z=0} = \frac{\lambda}{8} UU_m \\ \frac{1}{\rho_1} T_{yz}|_{z=0} = \frac{\lambda}{8} VU_m \end{cases} \tag{10}$$

where the friction factor  $\lambda$  for turbulent hydraulically fully-rough bed flows is given by the formula (Çengel and Cimbala, 2006):

$$\lambda = \frac{0.25}{\left[ \text{Log} \left( \frac{\varepsilon}{3.71 Hf} \right) \right]^2} \tag{11}$$

where  $f$  is a shape factor and  $\varepsilon/H$  is the relative roughness with respect to the total height of the two fluids.

The partial differential system (6) is written in conservative form and can be numerically solved by a finite-volume-based method, adopting the Godunov formulation with Roe approximate Riemann solver and treating the diffusive terms at right hand side of the fourth equations as source terms. An exhaustive explanation of the numerical approach is given in La Rocca et al. (2008).

As for the boundary conditions, no-flux conditions have been applied on the impermeable, rigid walls of the tank, i.e. the velocity component normal to the wall has been set to zero. As for the initial conditions, the numerical simulations started from a quiescent condition of the fluid mass: i.e. the initial velocity was set to zero everywhere while the initial depth of the heavy fluid mass was assumed as discontinuous. In particular, the depth of the heavy fluid mass at  $t = 0$  is equal to  $h_0$  for  $0 \leq x \leq L_0$ ,  $0 \leq y \leq b$  and equal to 0 for  $L_0 < x \leq L$ ,  $0 \leq y \leq b$ .

5 Analysis of numerical results

The runs listed in Table 1 were simulated by the mathematical model described in section 4

and numerical results were compared with the experimental ones. Figure 7 and Figure 8 show the top-view of the gravity current for all of the considered runs at three different times. Dotted lines represent the experimental front of the gravity current, obtained by means of the threshold method. Solid lines represent the numerical front of the gravity current, defined as the contour plot whose height is 0.01 m, which is a suitable value based on experimental observations. Figure 9 shows a typical numerical profile of the gravity current (Run 7) computed at the centreline of the tank, illustrating the definition of the front position at  $h = 0.01$  m used for the numerical results. The numerical gravity current exhibits a profile that smoothly decreases to zero at the bottom of the tank without showing a pronounced head. Each plot in Figs. 7 and 8 shows the current profile for the runs carried out with  $\delta = 0.101$  (i.e. Run 1, Run 4, Run 7, Run 10) at three different times, chosen in order to observe the whole duration of the experiments (i.e. until the interface reaches one of the lateral walls of the tank). The numerical results shown in Fig. 7 were obtained accounting for the entrainment in the numerical model, while in the numerical simulations reported in Fig. 8 the entrainment term was neglected. The comparisons are quite good if the entrainment is accounted for in the numerical model, as can be observed in Fig. 7, where the propagation of the numerical and experimental currents shows a satisfying agreement. On the contrary, when the entrainment is neglected (Fig. 8), the propagation of the numerical runs is slower than the experimental one.

In Figs. 10 and 11 time histories of the experimental and numerical front positions are plotted in dimensionless form. The time  $t$  and the front position  $x_f$  are scaled as in Fig. 5 (Section 3). In Figs. 10 and 11 laboratory data are compared with numerical results for miscible (i.e. entrainment of ambient fluid is accounted for in the numerical simulations) and immiscible (i.e. entrainment of ambient fluid is neglected in the numerical simulations) fluids, respectively. Regarding the case of miscible fluid (Fig. 10), experimental and numerical results show a quite good agreement, mainly appreciable for the low values of the parameter  $\delta$  ( $\delta = 0.101, 0.259$ , i.e. Fig. 10b-c-e-f). For the runs performed with the wider lock ( $\delta = 0.496$ ) the numerical simulations, carried out taking into account the entrainment, overestimate the propagation speed of the gravity current, as it can be observed in Figs. 10a and 10d. The simulations performed with the entrainment seem to satisfactorily predict the whole development of the experimental runs, as the time duration of the experiments carried out with the narrower and the intermediate lock widths (i.e.  $\delta = 0.101$  and  $0.259$ ) is long enough to allow the observation of a deceleration phase in the current dynamics. On the contrary, for the runs performed with the wider lock (i.e.  $\delta = 0.496$ ), only a linear constant phase can be observed in the front evolution and the mixing effects do not play an important role. In conclusion, the effect of the entrainment is important and permits accurate predictions of the gravity current propagation velocity for the cases with low values of  $\delta$  (i.e.  $\delta = 0.101$  and

1  
2  
3  
4  
5  
6  
7  
8  
9  
10  
11  
12  
13  
14  
15  
16  
17  
18  
19  
20  
21  
22  
23  
24  
25  
26  
27  
28  
29  
30  
31  
32  
33  
34  
35  
36  
37  
38  
39  
40  
41  
42  
43  
44  
45  
46  
47  
48  
49  
50  
51  
52  
53  
54  
55  
56  
57  
58  
59  
60

0.259). On the contrary, the effect of the entrainment is not important for the case with the largest value of  $\delta$  (i.e.  $\delta = 0.496$ ), at least for the adopted experimental configuration.

The opening of the lock can be related to the linear/nonlinear dependence of the front position with time: the nonlinear dependency becomes more and more evident for the cases with low values of  $\delta$  (i.e.  $\delta = 0.101$  and  $0.259$ ). A linear dependence of the front position with time means that the propagation velocity of the gravity current does not depend on time, while a nonlinear dependence of the front position with time means that this propagation velocity decreases with time. A time-independent propagation velocity occurs in the case with the largest  $\delta$  (i.e.  $\delta = 0.496$ ) as if the gravity current was able to develop the slumping phase. For the cases with low  $\delta$  (i.e.  $\delta = 0.101$  and  $0.259$ ), the lock choking effect on the flow causes an important loss of mechanical energy which probably introduces the development of a non-linear phase. In order to estimate the loss of mechanical energy, it is useful to introduce the dimensionless hydraulic head  $H_h^*$  of the dense current:

$$H_h^* = \frac{1}{H} \left( h_1 + \frac{U^2}{2g'_0} \right) \tag{12}$$

The relative difference between the hydraulic head evaluated upstream  $H_{hu}^*$  and downstream  $H_{hd}^*$  of the lock is computed as follows:

$$\Delta H_h^* = 100 \times \frac{H_{hu}^* - H_{hd}^*}{H_{hu}^*} \tag{13}$$

In order to quantify the concentrated loss of mechanical energy of the gravity current across the lock, the computed values for  $\Delta H_h^*$  are reported in Table 2 for all the numerical runs. The concentrated loss, due to the lock choking effect, is evident: the wider the lock, the smaller the loss and vice versa.

6 Conclusions

In this work, the dynamics of unconfined gravity currents was investigated both by laboratory experiments and numerical simulations. Twelve full-depth lock-exchange gravity currents were considered, varying the initial density of the heavier fluid, the initial height of the two fluid masses and the lock width. The effect of the variation of the lock width on the current dynamics represents a novelty of this work, as to the authors' knowledge it has not been investigated so far.

Numerical simulations were performed by means of a new single-layer, shallow-water model, able to account for the entrainment of ambient fluid in the gravity current. The experiments were realized in a Perspex tank, recording the evolution of the gravity current from the top by means of a digital camera. Images have been analysed and relevant quantities,

such as the gravity current profile and front position along the centreline were obtained. Results show that the front of the gravity current travels at a speed that depends on both the initial height and the initial gravity current density: the larger are the initial height and density of the lock fluid, the faster travels the front.

The role of the lock width was highlighted: the latter chokes the flow causing a concentrated loss of the mechanical energy of the gravity current. The smaller the lock width, the larger the concentrated loss. Indeed the results show that the currents produced with the wider gate develop a linear phase (i.e. propagation speed is constant along the tank centerline) while a non-linear phase occurs for the runs performed with a narrow gate: in this configuration, the flow decelerates and the length of the non-linear phase increases as the gate width decreases.

The role played by the entrainment in the numerical simulations is relevant. It was shown that the entrainment affects sensibly the propagation velocity of the gravity current front. This behaviour is particularly appreciable for the cases with small  $\delta$  (narrow lock).

### Acknowledgements

M.L.R. acknowledges financial support through the Italian national research grant “Hydroelectric energy by osmosis in coastal areas”, PRIN 2010-2011.

### Notation

$b$  = tank width (m)

$C$  = depth-averaged concentration of sodium chloride (-)

$d$  = lock width (m)

$F$  = Froude number (-)

$g$  = gravity acceleration ( $\text{ms}^{-2}$ )

$g_0'$  = initial reduced gravity ( $\text{ms}^{-2}$ )

$h_0$  = lock height (m)

$h_1$  = height of heavy fluid (m)

$H$  = total height of the two fluids (m)

$H_h^*$  = dimensionless hydraulic head of the dense current (-)

$H_{hd}^*$  = dimensionless hydraulic head evaluated downstream (-)

$H_{hu}^*$  = dimensionless hydraulic head evaluated upstream (-)

$H_t$  = tank height (m)

$k$  = dimensionless parameter in the entrainment formula (-)

$L$  = tank length (m)

$L_0$  = lock length (m)

$R_i$  = Reynolds number (-)  
 $t$  = time (s)  
 $T^*$  = dimensionless time (-)  
 $T_{xz}|_{z=0}, T_{yz}|_{z=0}$  = bottom stress terms (Pa)  
 $U_0$  = buoyancy velocity ( $\text{ms}^{-1}$ )  
 $U$  = depth-averaged velocity along  $x$  axis ( $\text{ms}^{-1}$ )  
 $U_m$  = velocity modulus ( $\text{ms}^{-1}$ )  
 $V$  = depth-averaged velocity along  $y$  axis ( $\text{ms}^{-1}$ )  
 $x, y, z$  = space variables (m)  
 $x_f$  = front position (m)  
 $x_f^*$  = dimensionless front position (-)  
 $\alpha$  = entrainment coefficient (-)  
 $\gamma$  = density ratio (-)  
 $\delta$  = width ratio (-)  
 $\lambda$  = friction factor (-)  
 $\nu$  = kinematic viscosity ( $\text{m}^2\text{s}^{-1}$ )  
 $\rho_{01}$  = initial density of heavy fluid ( $\text{kgm}^{-3}$ )  
 $\rho_1$  = density of heavy fluid ( $\text{kgm}^{-3}$ )  
 $\rho_2$  = density of ambient fluid ( $\text{kgm}^{-3}$ )  
 $\rho_s$  = density of sodium chloride ( $\text{kgm}^{-3}$ )

**References**

Adduce, C., Sciortino, G., & Proietti, S. (2012). Gravity currents produced by lock-exchange: experiments and simulations with a two layer shallow-water model with entrainment. *Journal of Hydraulic Engineering*, 138(2), 111-121.

Baines, P.G. (2001). Mixing in flows down gentle slopes into stratified environments. *Journal of Fluid Mechanics*, 443, 237-270.

Baines, P.G. (2005). Mixing regimes for the flow of dense fluid down slopes into stratified environments. *Journal of Fluid Mechanics*, 538, 245-267.

Bombardelli, F.A., Cantero, M.I., Garcia, M.H., & Buscaglia, G.C. (2009). Numerical aspect of the simulation of discontinuous saline underflows: the lock-exchange problem. *Journal of Hydraulic Research*, 47(6), 777-789.

- Cantero, M., Balachandar, S., García, M.H., & Ferry, J. (2006). Direct numerical simulations of planar and cylindrical density currents. *Journal of Applied Mechanics*, 73(6), 923-930.
- Cantero, M., Balachandar, S., & García, M.H. (2007). High-resolution simulations of cylindrical density currents. *Journal of Fluid Mechanics*, 590, 437-469.
- Cenedese, C., & Adduce, C. (2008). Mixing in a density-driven current flowing down a slope in a rotating fluid. *Journal of Fluid Mechanics*, 604, 369-388.
- Cenedese, C., & Adduce, C. (2010). A new entrainment parameterization for mixing in overflows. *Journal of Physical Oceanography*, 40(8), 1835-1850.
- Çengel, Y.A., & Cimbala, J.M. (2006). *Fluid Mechanics: fundamentals and applications*. New York: Mac Graw Hill.
- Dai, A. (2013). Experiments on gravity currents propagating on different bottom slopes. *Journal of Fluid Mechanics*, 731, 117-141.
- Dai, A. (2015). High-resolution simulations of downslope gravity currents in the acceleration phase. *Physics of Fluids*, 27 (7), 076602.
- Gonzalez-Juez, E., Meiburg, E., & Constantinescu, G. (2009). Gravity currents impinging on bottom-mounted square cylinders: flow fields and associated forces. *Journal of Fluid Mechanics*, 631, 65-102.
- Huppert, H.E. (2006). Gravity currents: a personal perspective. *Journal of Fluid Mechanics*, 554, 299-322.
- Huppert, H.E., & Simpson, J.E. (1980). The slumping of gravity currents. *Journal of Fluid Mechanics*, 99, 785-799.
- Kneller, B., & Buckee, C. (2000). The structure and fluid mechanics of turbidity currents: a review of some recent studies and their geological implications. *Sedimentology*, 47, 62-94.

1  
2  
3  
4  
5  
6  
7  
8  
9  
10  
11  
12  
13  
14  
15  
16  
17  
18  
19  
20  
21  
22  
23  
24  
25  
26  
27  
28  
29  
30  
31  
32  
33  
34  
35  
36  
37  
38  
39  
40  
41  
42  
43  
44  
45  
46  
47  
48  
49  
50  
51  
52  
53  
54  
55  
56  
57  
58  
59  
60

La Rocca, M., Adduce, C., Sciortino, G., Bateman Pinzon, A. & Boniforti, M. A. (2012a). A two-layer shallow water model for 3D gravity currents. *Journal of Hydraulic Research*, 50(2), 208-217

La Rocca, M., Adduce, C., Lombardi, V., Sciortino, G., & Hinkelmann, R. (2012b). Development of a lattice Boltzmann method for two-layered shallow-water flow. *International Journal for Numerical Methods in Fluids*, 70(8), 1048-1072.

La Rocca, M., Adduce, C., Sciortino, G., & Bateman Pinzon, A. (2008). Experimental and numerical simulation of three-dimensional gravity currents on smooth and rough bottom. *Physics of Fluids*, 20(10), 106603.

La Rocca, M., Prestininzi, P., Adduce, C., Sciortino, G., & Hinkelmann, R. (2013). Lattice Boltzmann simulation of 3D gravity currents around obstacles. *International Journal of Offshore and Polar Engineering*, 23(3), 178–185.

Lombardi, V., Adduce, C., Sciortino, G., & La Rocca, M., (2015). Gravity currents flowing upslope: Laboratory experiments and shallow-water simulations. *Physics of Fluids*, 27(1), 016602.

Marleau, L.J., Flynn M.R., & Sutherland B.R. (2014). Gravity currents propagating up a slope. *Physics of Fluids*, 26(4), 046605.

Nogueira, H.I.S, Adduce, C., Alves, E., & Franca, M.J. (2013). Analysis of lock-exchange gravity currents over smooth and rough beds. *Journal of Hydraulic Research*, 51(4), 417-431.

Nogueira, H.I.S, Adduce, C., Alves, E., & Franca, M.J. (2014). Dynamics of the head of gravity currents. *Environmental Fluid Mechanics*, 14(2), 519-540.

Ooi, S.K., Costantinescu, G., & Weber, L.J. (2009). Numerical simulations of lock-exchange compositional gravity current. *Journal of Fluid Mechanics*, 635, 361-388.

Ottolenghi, L., Adduce, C., Inghilesi, R., Armenio, V., & Roman, F. (2016a). Entrainment and mixing in unsteady gravity currents. *Journal of Hydraulic Research*, 54(5), 541-557.



- Ottolenghi, L., Adduce, C., Inghilesi, R., Roman, F., & Armenio, V. (2016b). Mixing in lock-release gravity currents propagating up a slope. *Physics of Fluids*, 28(5), 056604.
- Ottolenghi, L., Cenedese, C., & Adduce, C. (2017a). Entrainment in a dense current flowing down a rough sloping bottom in a rotating fluid. *Journal of Physical Oceanography*, 47(3), 485-498.
- Ottolenghi L., Adduce C., Roman F., & Armenio V. (2017b) Analysis of the flow in gravity currents propagating up a slope. *Ocean Modelling*, 115, 1-13. DOI: 10.1016/j.ocemod.2017.05.001.
- Patterson, M.D., Simpson J.E. & Dalziel S.B. (2006). Vortical motion in the head of an axisymmetric gravity current. *Physics of Fluids*, 18(4), 046601.
- Prestininzi, P., Sciortino, G., & La Rocca, M. (2013). On the effect of the intrinsic viscosity in a 2-layer shallow water lattice Boltzmann model of axisymmetric density currents. *Journal of Hydraulic Research*, 51(6), 668-680.
- Prestininzi, P., Sciortino, G., & La Rocca, M. (2014). Comparative Study of a Boltzmann-based Finite Volume and a Lattice Boltzmann Model for Shallow Water Flows in Complex Domains. *International Journal of Offshore and Polar Engineering*, 24(3), 161-167.
- Ross, A.N., Linden, P.F., & Dalziel, S.B. (2002). A study of three dimensional gravity currents on a uniform slope. *Journal of Fluid Mechanics*, 453, 239-261.
- Rottmann, J. W. & Simpson, J.E. (1983). Gravity currents produced by instantaneous release of a heavy fluid in a rectangular channel. *Journal of Fluid Mechanics*, 14, 95-110.
- Sciortino, G., Adduce, C., & Lombardi, V. (2017). A new front condition for non-Boussinesq gravity currents. *Journal of Hydraulic Research* (accepted).
- Shin, J.O., Dalziel, S.B., & Linden, P.F. (2004). Gravity currents produced by lock exchange. *Journal of Fluid Mechanics*, 521, 1-34.
- Simpson, J.E. (1997). *Gravity currents in the environment and the laboratory*. Cambridge: Cambridge University Press.

1  
2  
3  
4  
5  
6  
7  
8  
9  
10  
11  
12  
13  
14  
15  
16  
17  
18  
19  
20  
21  
22  
23  
24  
25  
26  
27  
28  
29  
30  
31  
32  
33  
34  
35  
36  
37  
38  
39  
40  
41  
42  
43  
44  
45  
46  
47  
48  
49  
50  
51  
52  
53  
54  
55  
56  
57  
58  
59  
60

Tokyay, T., Constantinescu, G., & Meiburg, E. (2011). Lock-exchange gravity currents with a high volume of release propagating over a periodic array of obstacles. *Journal of Fluid Mechanics*, 672, 570-605.

Ungarish, M. (2009). *An introduction to gravity currents and intrusions*. Boca Raton, FL, USA: CRC Press.

Van Meerkerk, M., O’Mahoney, T., & Twerda, A. (2015, July). *Development of a CDF model of an air curtain for saltwater intrusion prevention*. Paper presented at the 36<sup>th</sup> IAHR World Congress, Delft-The Hague, the Netherlands.

Yuan, Y., & Horner-Devine, A.R. (2013). Laboratory investigation of the impact of lateral spreading on buoyancy flux in a river plume. *Journal of Physical Oceanography*, 43(12), 2588-2610.

Table 1 Initial experimental conditions.

Run	$h_0$	$\rho_{01}$	$\rho_2$	$d$	$\gamma$	$\delta$	$g_0'$	$U_0$	$R_i$
	(m)	(kgm <sup>-3</sup> )	(kgm <sup>-3</sup> )	(m)	(-)	(-)	(ms <sup>-2</sup> )	(ms <sup>-1</sup> )	(-)
1	0.15	1010	1001	0.136	0.99	0.101	0.09	0.11	17253
2	0.15	1010	1001	0.350	0.99	0.259	0.09	0.11	17253
3	0.15	1010	1001	0.670	0.99	0.496	0.09	0.11	17253
4	0.10	1010	1002	0.136	0.99	0.101	0.08	0.09	8850
5	0.10	1010	1001	0.350	0.99	0.259	0.09	0.09	9392
6	0.10	1010	1000	0.670	0.99	0.496	0.10	0.10	9905
7	0.15	1030	1001	0.136	0.97	0.101	0.28	0.21	30971
8	0.15	1030	1002	0.350	0.97	0.259	0.27	0.20	30417
9	0.15	1030	1001	0.670	0.97	0.496	0.28	0.21	30971
10	0.10	1030	1002	0.136	0.97	0.101	0.27	0.17	16557
11	0.10	1030	1002	0.350	0.97	0.259	0.27	0.17	16557
12	0.10	1030	1002	0.670	0.97	0.496	0.27	0.17	16557

1  
2  
3  
4  
5  
6  
7  
8  
9  
10  
11  
12  
13  
14  
15  
16  
17  
18  
19  
20  
21  
22  
23  
24  
25  
26  
27  
28  
29  
30  
31  
32  
33  
34  
35  
36  
37  
38  
39  
40  
41  
42  
43  
44  
45  
46  
47  
48  
49  
50  
51  
52  
53  
54  
55  
56  
57  
58  
59  
60

Table 2 Values of relative difference of hydraulic head computed for all the runs by equation (13).

Run	$h_0$	$\rho_{01}$	$\Delta H_h^*$	$\delta$
	(m)	(kgm <sup>-3</sup> )	(-)	(-)
1	0.15	1010	44.8	0.101
2	0.15	1010	25.1	0.259
3	0.15	1010	16.2	0.496
4	0.10	1010	48.1	0.101
5	0.10	1010	28.9	0.259
6	0.10	1010	19.0	0.496
7	0.15	1030	45.5	0.101
8	0.15	1030	25.3	0.259
9	0.15	1030	16.3	0.496
10	0.10	1030	49.0	0.101
11	0.10	1030	29.3	0.259
12	0.10	1030	19.2	0.496

**Figures captions:**

Figure 1 Sketch of the lock-release tank: (a) top view; (b) side view.

Figure 2 Typical development of a laboratory gravity current (Run 10) at  $t = 3$  s (a),  $t = 7$  s (b),  $t = 11$  s (c). White arrows indicate the portion behind the billow at the current front.

Figure 3 Effect of the initial height and excess density on the propagation of an unconfined gravity current: comparison between Run 2 and Run 5 for  $t = 5$  s (a),  $t = 10$  s (b),  $t = 14$  s (c); comparison between Run 8 and Run 2 for  $t = 3$  s (d),  $t = 6$  s (e),  $t = 9$  s (f).

Figure 4 Effect of the lock width: comparison between Run 9, Run 8 and Run 7 for  $t = 3$  s (a),  $t = 5$  s (b),  $t = 14$  s (c); comparison between Run 6, Run 5 and Run 4 for  $t = 6$  s (d),  $t = 11$  s (e),  $t = 16$  s (f).

Figure 5 Dimensionless plot of experimental front positions versus time along the centreline of the tank: (a) Run 1 ( $d = 0.136$  m), Run 2 ( $d = 0.35$  m), Run 3 ( $d = 0.67$  m); (b) Run 4 ( $d = 0.136$  m), Run 5 ( $d = 0.35$  m), Run 6 ( $d = 0.67$  m); (c) Run 7 ( $d = 0.136$  m), Run 8 ( $d = 0.35$  m), Run 9 ( $d = 0.67$  m); (d) Run 10 ( $d = 0.136$  m), Run 11 ( $d = 0.35$  m), Run 12 ( $d = 0.67$  m).

Figure 6 Sketch of the gravity current.

Figure 7 Comparison between experimental current profile (dots) and numerical predictions (solid line) obtained taking into account the entrainment for the runs performed with  $d = 0.136$  m at three different instants of time. (a) Run 1:  $\rho_{01} = 1010$  kg/m<sup>3</sup>,  $h_0 = 0.15$  m (b) Run 4:  $\rho_{01} = 1010$  kg/m<sup>3</sup>,  $h_0 = 0.10$  m (c) Run 7:  $\rho_{01} = 1030$  kg/m<sup>3</sup>,  $h_0 = 0.15$  m (f) Run 10:  $\rho_{01} = 1030$  kg/m<sup>3</sup>,  $h_0 = 0.15$  m.

Figure 8 Comparison between experimental current profile (dots) and numerical predictions (solid line) obtained neglecting the entrainment in the numerical simulations for the runs performed with  $d = 0.136$  m at three different instants of time. (a) Run 1:  $\rho_{01} = 1010$  kg/m<sup>3</sup>,  $h_0 = 0.15$  m (b) Run 4:  $\rho_{01} = 1010$  kg/m<sup>3</sup>,  $h_0 = 0.10$  m (c) Run 7:  $\rho_{01} = 1030$  kg/m<sup>3</sup>,  $h_0 = 0.15$  m (f) Run 10:  $\rho_{01} = 1030$  kg/m<sup>3</sup>,  $h_0 = 0.15$  m.

1  
2  
3  
4  
5  
6  
7  
8  
9  
10  
11  
12  
13  
14  
15  
16  
17  
18  
19  
20  
21  
22  
23  
24  
25  
26  
27  
28  
29  
30  
31  
32  
33  
34  
35  
36  
37  
38  
39  
40  
41  
42  
43  
44  
45  
46  
47  
48  
49  
50  
51  
52  
53  
54  
55  
56  
57  
58  
59  
60

Figure 9 Numerical profile computed on the centreline of the tank for Run 7 ( $\rho_{01} = 1030$  kg/m<sup>3</sup>,  $h_0 = 0.15$  m) at  $t = 3$  s after the removal of the gate.

Figure 10 Comparison between experimental data (symbols) and numerical simulation (lines) performed taking into account the entrainment: dimensionless plots of front positions versus time along the centreline of the tank. (a) Run 9 ( $\rho_{01} = 1030$  kg/m<sup>3</sup>), Run 3 ( $\rho_{01} = 1010$  kg/m<sup>3</sup>), (b) Run 8 ( $\rho_{01} = 1030$  kg/m<sup>3</sup>), Run 2 ( $\rho_{01} = 1010$  kg/m<sup>3</sup>), (c) Run 7 ( $\rho_{01} = 1030$  kg/m<sup>3</sup>), Run 1 ( $\rho_{01} = 1010$  kg/m<sup>3</sup>), (d) Run 12 ( $\rho_{01} = 1030$  kg/m<sup>3</sup>), Run 6 ( $\rho_{01} = 1010$  kg/m<sup>3</sup>), (e) Run 11 ( $\rho_{01} = 1030$  kg/m<sup>3</sup>), Run 5 ( $\rho_{01} = 1010$  kg/m<sup>3</sup>), (f) Run 10 ( $\rho_{01} = 1030$  kg/m<sup>3</sup>), Run 4 ( $\rho_{01} = 1010$  kg/m<sup>3</sup>).

Figure 11 Comparison between experimental data (symbols) and numerical simulation (lines) performed neglecting the entrainment: dimensionless plots of front positions versus time along the centreline of the tank. (a) Run 9 ( $\rho_{01} = 1030$  kg/m<sup>3</sup>), Run 3 ( $\rho_{01} = 1010$  kg/m<sup>3</sup>), (b) Run 8 ( $\rho_{01} = 1030$  kg/m<sup>3</sup>), Run 2 ( $\rho_{01} = 1010$  kg/m<sup>3</sup>), (c) Run 7 ( $\rho_{01} = 1030$  kg/m<sup>3</sup>), Run 1 ( $\rho_{01} = 1010$  kg/m<sup>3</sup>), (d) Run 12 ( $\rho_{01} = 1030$  kg/m<sup>3</sup>), Run 6 ( $\rho_{01} = 1010$  kg/m<sup>3</sup>), (e) Run 11 ( $\rho_{01} = 1030$  kg/m<sup>3</sup>), Run 5 ( $\rho_{01} = 1010$  kg/m<sup>3</sup>), (f) Run 10 ( $\rho_{01} = 1030$  kg/m<sup>3</sup>), Run 4 ( $\rho_{01} = 1010$  kg/m<sup>3</sup>).

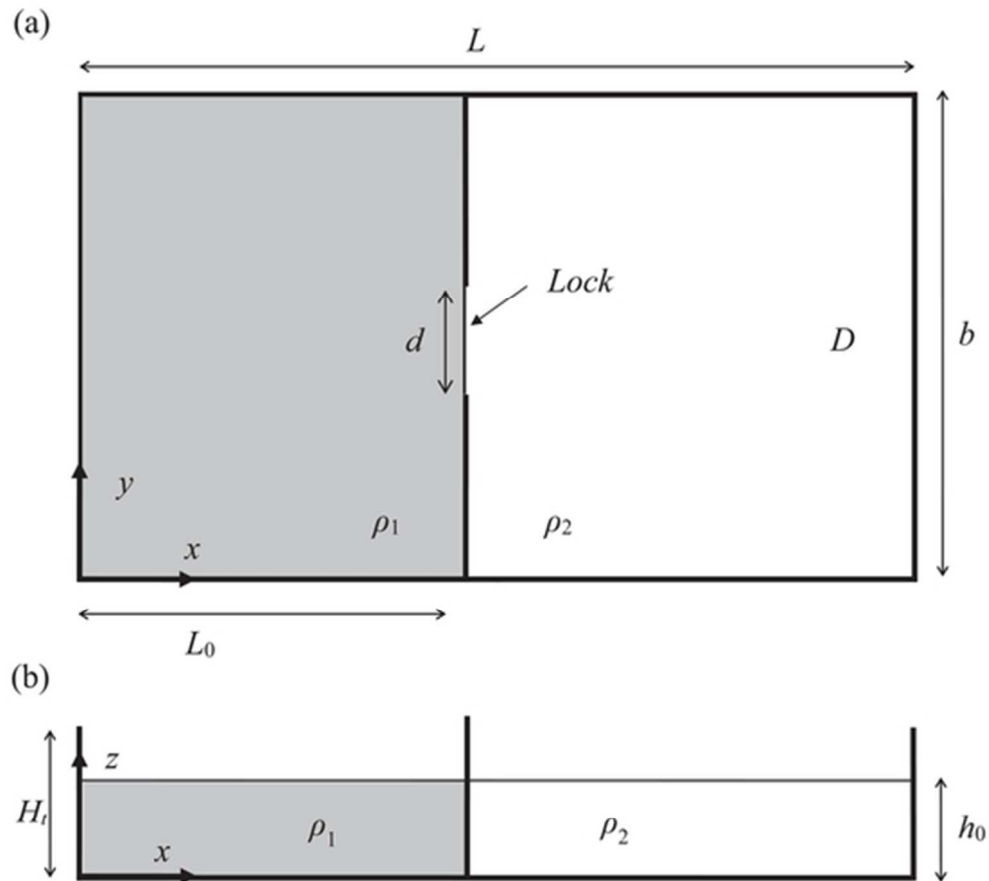


Figure 1 Sketch of the lock-release tank: (a) top view; (b) side view.

47x44mm (300 x 300 DPI)

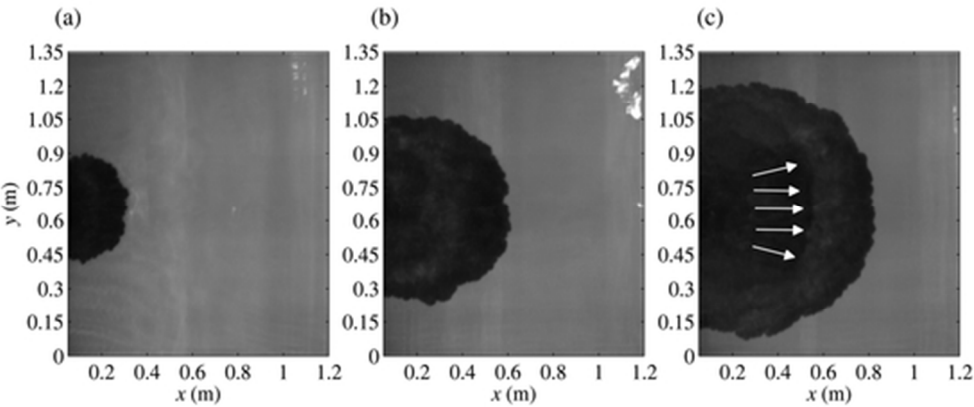


Figure 2 Typical development of a laboratory gravity current (Run 10) at  $t = 3$  s (a),  $t = 7$  s (b),  $t = 11$  s (c). White arrows indicate the portion behind the billow at the current front.

47x19mm (300 x 300 DPI)



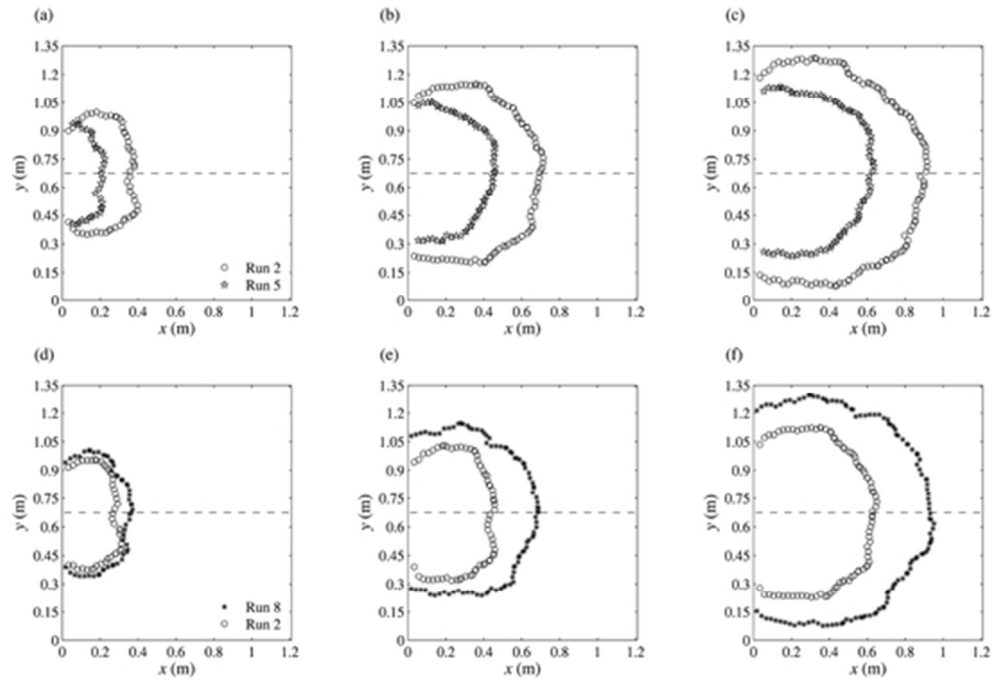


Figure 3 Effect of the initial height and excess density on the propagation of an unconfined gravity current: comparison between Run 2 and Run 5 for  $t = 5$  s (a),  $t = 10$  s (b),  $t = 14$  s (c); comparison between Run 8 and Run 2 for  $t = 3$  s (d),  $t = 6$  s (e),  $t = 9$  s (f).

47x32mm (300 x 300 DPI)

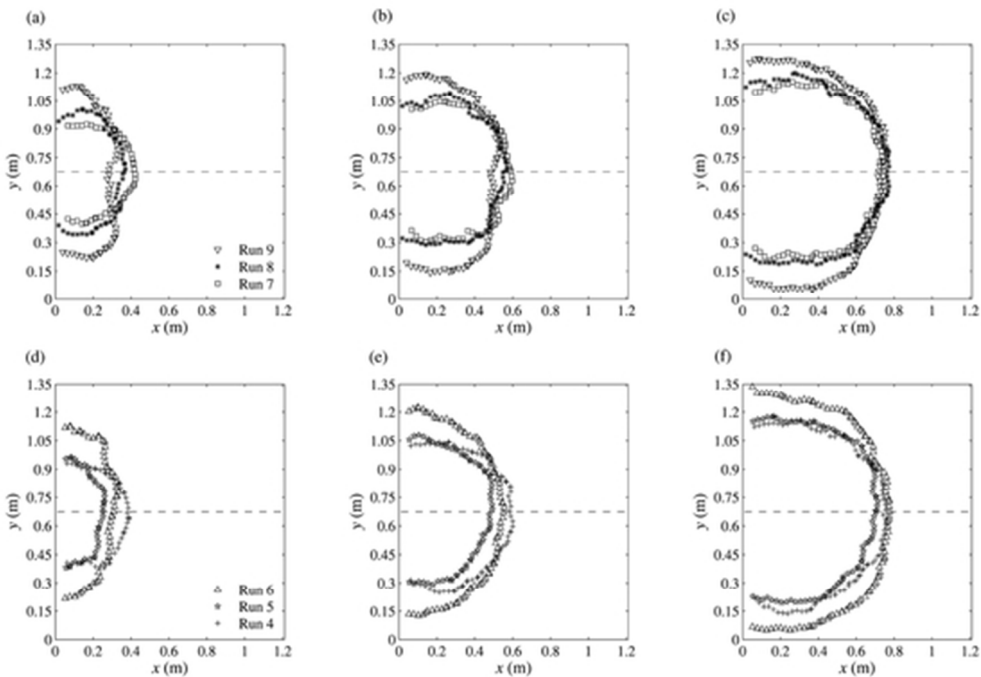


Figure 4 Effect of the lock width: comparison between Run 9, Run 8 and Run 7 for  $t = 3$  s (a),  $t = 5$  s (b),  $t = 14$  s (c); comparison between Run 6, Run 5 and Run 4 for  $t = 6$  s (d),  $t = 11$  s (e),  $t = 16$  s (f).

47x32mm (300 x 300 DPI)

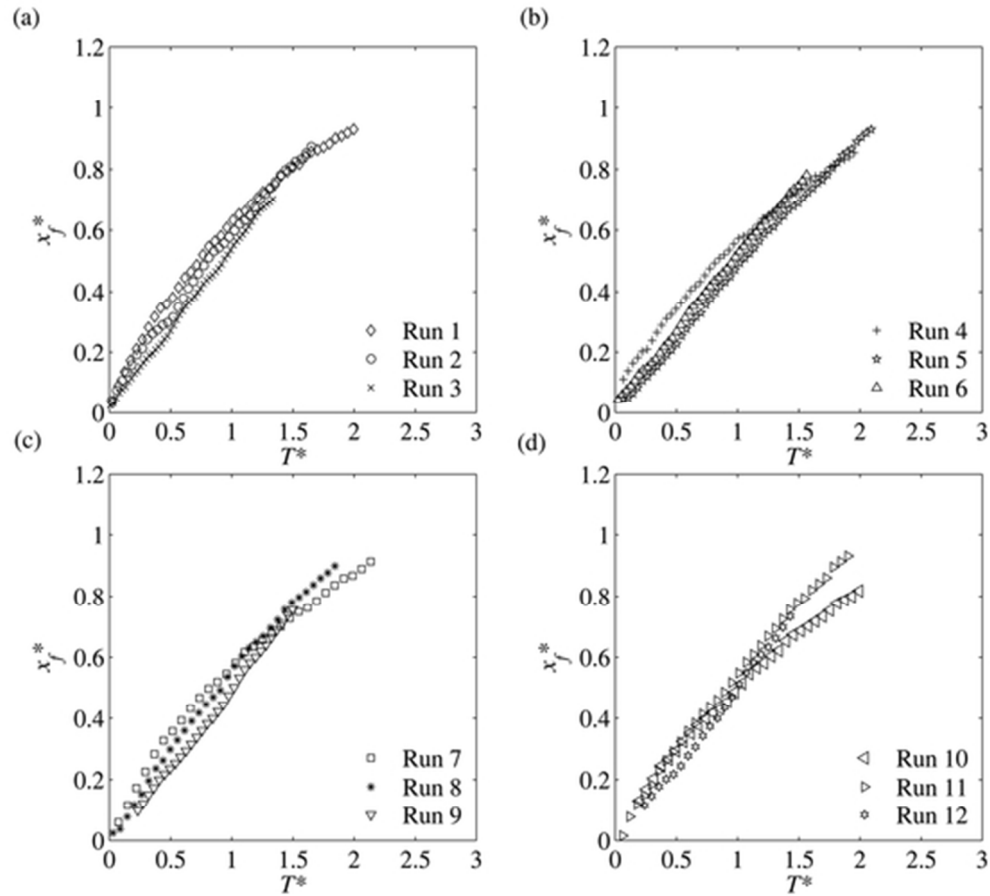


Figure 5 Dimensionless plot of experimental front positions versus time along the centreline of the tank: (a) Run 1 ( $d = 0.136$  m), Run 2 ( $d = 0.35$  m), Run 3 ( $d = 0.67$  m); (b) Run 4 ( $d = 0.136$  m), Run 5 ( $d = 0.35$  m), Run 6 ( $d = 0.67$  m); (c) Run 7 ( $d = 0.136$  m), Run 8 ( $d = 0.35$  m), Run 9 ( $d = 0.67$  m); (d) Run 10 ( $d = 0.136$  m), Run 11 ( $d = 0.35$  m), Run 12 ( $d = 0.67$  m).

47x42mm (300 x 300 DPI)

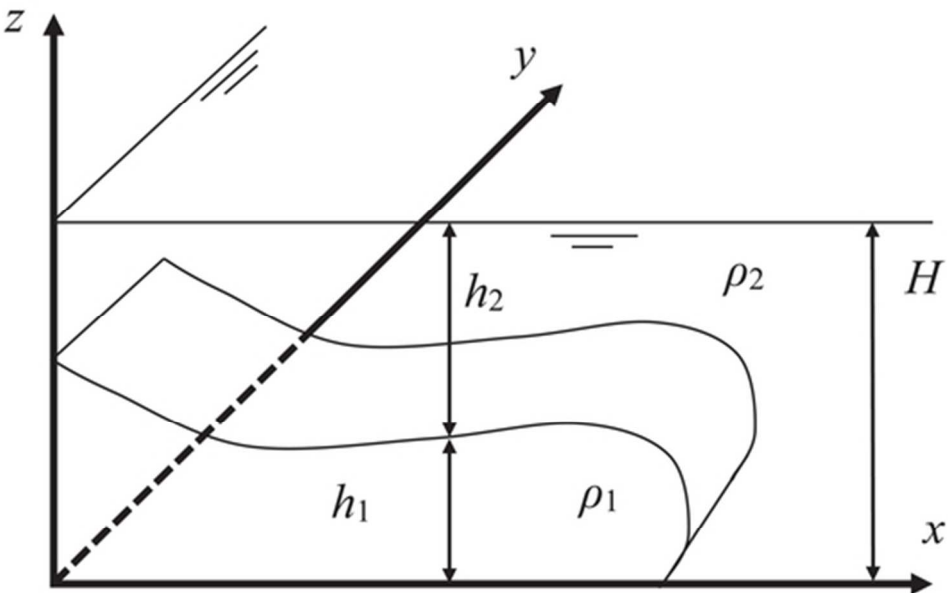


Figure 6 Sketch of the gravity current.

47x30mm (300 x 300 DPI)

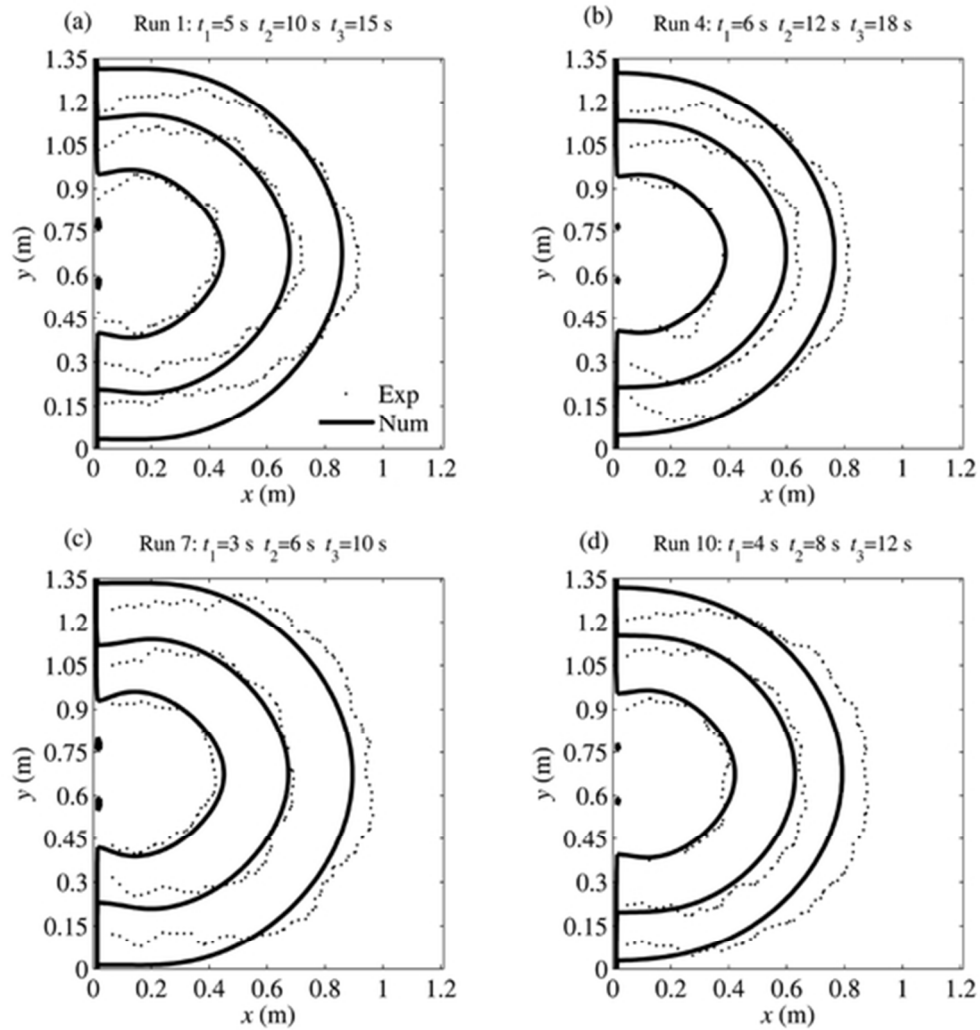


Figure 7 Comparison between experimental current profile (dots) and numerical predictions (solid line) obtained taking into account the entrainment for the runs performed with  $d = 0.136$  m at three different instants of time. (a) Run 1:  $\rho_{01} = 1010$  kg/m<sup>3</sup>,  $h_0 = 0.15$  m (b) Run 4:  $\rho_{01} = 1010$  kg/m<sup>3</sup>,  $h_0 = 0.10$  m (c) Run 7:  $\rho_{01} = 1030$  kg/m<sup>3</sup>,  $h_0 = 0.15$  m (d) Run 10:  $\rho_{01} = 1030$  kg/m<sup>3</sup>,  $h_0 = 0.15$  m.

47x49mm (300 x 300 DPI)

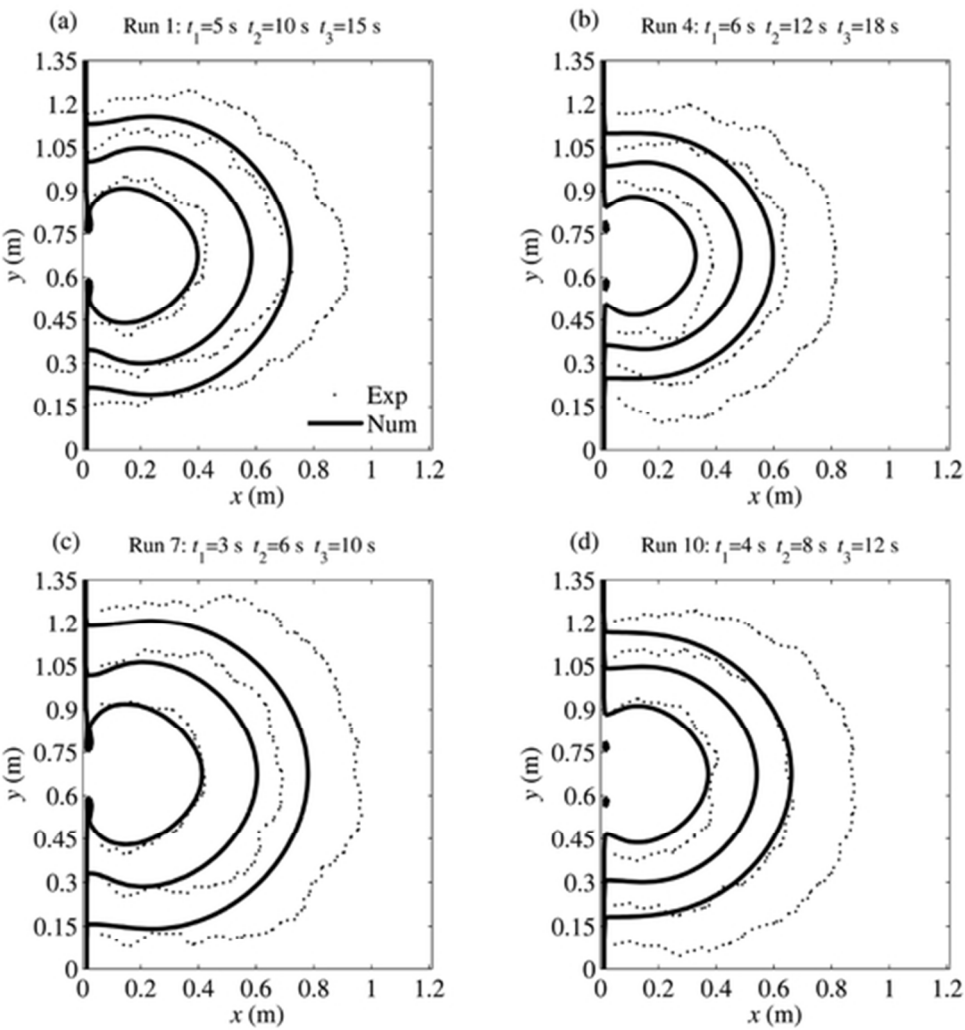


Figure 8 Comparison between experimental current profile (dots) and numerical predictions (solid line) obtained neglecting the entrainment in the numerical simulations for the runs performed with  $d = 0.136$  m at three different instants of time. (a) Run 1:  $\rho_{01} = 1010$  kg/m<sup>3</sup>,  $h_0 = 0.15$  m (b) Run 4:  $\rho_{01} = 1010$  kg/m<sup>3</sup>,  $h_0 = 0.10$  m (c) Run 7:  $\rho_{01} = 1030$  kg/m<sup>3</sup>,  $h_0 = 0.15$  m (f) Run 10:  $\rho_{01} = 1030$  kg/m<sup>3</sup>,  $h_0 = 0.15$  m.

47x49mm (300 x 300 DPI)

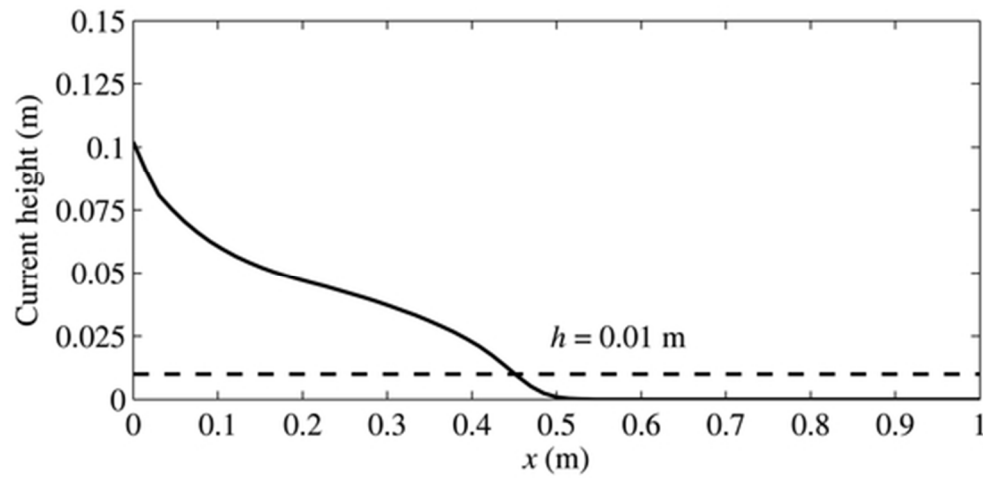


Figure 9 Numerical profile computed on the centreline of the tank for Run 7 ( $\rho_0 = 1030 \text{ kg/m}^3$ ,  $h_0 = 0.15 \text{ m}$ ) at  $t = 3 \text{ s}$  after the removal of the gate.

47x24mm (300 x 300 DPI)

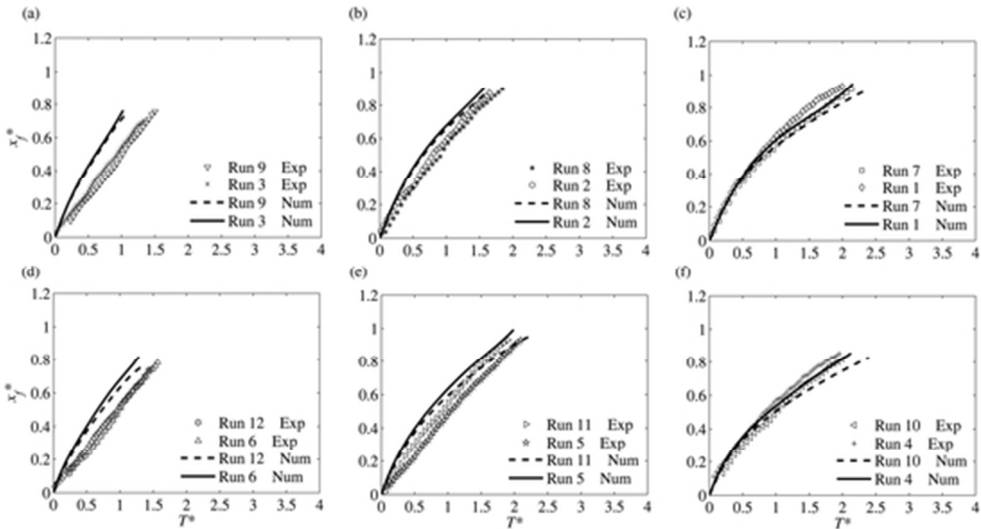


Figure 10 Comparison between experimental data (symbols) and numerical simulation (lines) performed taking into account the entrainment: dimensionless plots of front positions versus time along the centreline of the tank. (a) Run 9 ( $\rho_{01} = 1030 \text{ kg/m}^3$ ), Run 3 ( $\rho_{01} = 1010 \text{ kg/m}^3$ ), (b) Run 8 ( $\rho_{01} = 1030 \text{ kg/m}^3$ ), Run 2 ( $\rho_{01} = 1010 \text{ kg/m}^3$ ), (c) Run 7 ( $\rho_{01} = 1030 \text{ kg/m}^3$ ), Run 1 ( $\rho_{01} = 1010 \text{ kg/m}^3$ ), (d) Run 12 ( $\rho_{01} = 1030 \text{ kg/m}^3$ ), Run 6 ( $\rho_{01} = 1010 \text{ kg/m}^3$ ), (e) Run 11 ( $\rho_{01} = 1030 \text{ kg/m}^3$ ), Run 5 ( $\rho_{01} = 1010 \text{ kg/m}^3$ ), (f) Run 10 ( $\rho_{01} = 1030 \text{ kg/m}^3$ ), Run 4 ( $\rho_{01} = 1010 \text{ kg/m}^3$ ).

47x25mm (300 x 300 DPI)



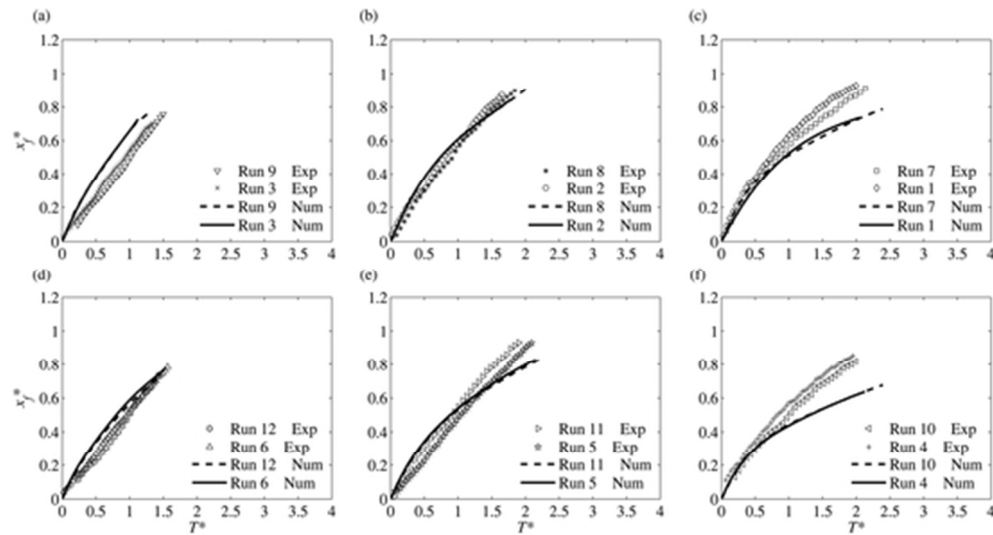


Figure 11 Comparison between experimental data (symbols) and numerical simulation (lines) performed neglecting the entrainment: dimensionless plots of front positions versus time along the centreline of the tank. (a) Run 9 ( $\rho_{01} = 1030 \text{ kg/m}^3$ ), Run 3 ( $\rho_{01} = 1010 \text{ kg/m}^3$ ), (b) Run 8 ( $\rho_{01} = 1030 \text{ kg/m}^3$ ), Run 2 ( $\rho_{01} = 1010 \text{ kg/m}^3$ ), (c) Run 7 ( $\rho_{01} = 1030 \text{ kg/m}^3$ ), Run 1 ( $\rho_{01} = 1010 \text{ kg/m}^3$ ), (d) Run 12 ( $\rho_{01} = 1030 \text{ kg/m}^3$ ), Run 6 ( $\rho_{01} = 1010 \text{ kg/m}^3$ ), (e) Run 11 ( $\rho_{01} = 1030 \text{ kg/m}^3$ ), Run 5 ( $\rho_{01} = 1010 \text{ kg/m}^3$ ), (f) Run 10 ( $\rho_{01} = 1030 \text{ kg/m}^3$ ), Run 4 ( $\rho_{01} = 1010 \text{ kg/m}^3$ ).

47x25mm (300 x 300 DPI)